

## ARTICLE OPEN



# High-efficiency microwave-optical quantum transduction based on a cavity electro-optic superconducting system with long coherence time

Changqing Wang<sup>1</sup>, Ivan Gonin<sup>1</sup>, Anna Grassellino<sup>1</sup>, Sergey Kazakov<sup>1</sup>, Alexander Romanenko<sup>1</sup>, Vyacheslav P. Yakovlev<sup>1</sup> and Silvia Zorzetti<sup>1</sup>✉

Frequency conversion between microwave and optical photons is a key enabling technology to create links between superconducting quantum processors and to realize distributed quantum networks. We propose a microwave-optical transduction platform based on long-coherence time superconducting radio-frequency (SRF) cavities coupled to electro-optic optical cavities to mitigate the loss mechanisms that limit the attainment of high conversion efficiency. We optimize the microwave-optical field overlap and optical coupling losses in the design while achieving long microwave and optical photon lifetime at milli-Kelvin temperatures. This represents a significant enhancement of the transduction efficiency up to 50% under incoming pump power of 140  $\mu$ W, which allows the conversion of few-photon quantum signals. Furthermore, this scheme exhibits high resolution for optically reading out the dispersive shift induced by a superconducting transmon qubit coupled to the SRF cavity. We also show that low microwave losses enhance the fidelity of heralded entanglement generation between two remote quantum systems. Finally, high precision in quantum sensing can be reached below the standard quantum limit.

npj Quantum Information (2022)8:149; <https://doi.org/10.1038/s41534-022-00664-7>

## INTRODUCTION

In the past decade, quantum information science and technology have been greatly boosted by the advancement of superconducting circuits<sup>1–3</sup>. However, the cryogenic temperature requirement restricts the capability to transfer quantum information between local quantum processors and, therefore, to build large-scale quantum networks<sup>4</sup>. Optical photons operating at a frequency of hundreds of Tera-Hertz (THz) are immune to thermal noise at room temperature and can be transferred distantly via the free-space and fiber communication technologies. As a result, optics has shown great promise for quantum communication and for connecting distant quantum nodes<sup>5</sup>. Quantum transducers are required to mediate the huge energy gap between microwave and optical photons, about five orders of magnitude, and therefore to integrate optical communication systems with superconducting quantum devices<sup>6–8</sup>.

Past years have witnessed extensive explorations of microwave-optical quantum transduction based on various kinds of hybrid platforms, including electro-optomechanics<sup>9,10</sup>, piezo-optomechanics<sup>11–14</sup>, magnonics<sup>15–18</sup>, atoms<sup>19–21</sup>, rare-earth ions<sup>22,23</sup>, electro-optic nonlinear materials<sup>24–29</sup>, and others. Among them, the electro-optic effect provides the most direct way to couple microwave and optical fields. The optical refractive index is modulated by the microwave electric field through the second-order electro-optic nonlinearity ( $\chi^{(2)}$ )<sup>30,31</sup>. As a result, frequency conversion has been demonstrated based on microwave cavities integrated with nonlinear optical resonators made of electro-optic materials such as lithium niobate (LN)<sup>32</sup> and aluminum nitride (AlN)<sup>33</sup>. In particular, the advancement of thin-film LN enables the fabrication of LN optical resonators with ultrahigh optical quality<sup>34</sup>, offering a promising platform for microwave-optical frequency conversion<sup>25–29</sup>. Yet, the small mode volume leads to overheating the devices when the pump

power applied to the optical resonator is high. Thus, the trade-off between the thermal noise<sup>35,36</sup> and transduction efficiency makes it hard to realize a high-efficiency quantum transducer operating near the quantum threshold. Not long ago, three-dimensional (3D) cavities were exploited for transduction with bulk LN crystal optical resonators embedded, where the large mode volume gives rise to larger pump power tolerance<sup>35–39</sup>. Pioneer work shows 0.03% photon conversion efficiency and 1.1 added output noise photons per second at 1.48 mW pump power<sup>37</sup>, demonstrating how three-dimensional geometries are transformative in quantum transduction, reducing the detrimental effect of thermally induced quasiparticles in the frequency conversion process. So far, the transduction efficiency is limited by the low-quality factor (Q) of the microwave resonators and by the non-optimal alignment between the microwave and optical mode distributions.

Three-dimensional bulk niobium superconducting cavities provide opportunities to mitigate quantum decoherence mechanisms<sup>40–43</sup>. Such cavities developed at Fermilab for particle accelerators exhibit record-long photon lifetime at milli-Kelvin (mK) temperature and thus mitigate the loss of microwave photons and greatly enhance light-matter interaction in the quantum regime. Moreover, the flexibility in cavity design and geometry offers degrees of freedom in modes selection and microwave engineering to fulfill different goals and requirements. In addition, the large vacuum space in the mode volume allows the integration with various other materials for achieving hybrid quantum systems with rich functionalities.

In this paper, we propose a high-efficiency, low-pump-power quantum transducer based on a three-dimensional architecture with a bulk niobium superconducting cavity integrated with an LN optical resonator. We maximize the microwave-optical interaction by careful RF design and optimization of the overlap between the

<sup>1</sup>Fermi National Accelerator Laboratory, Batavia, IL, USA. ✉email: zorzetti@fnal.gov

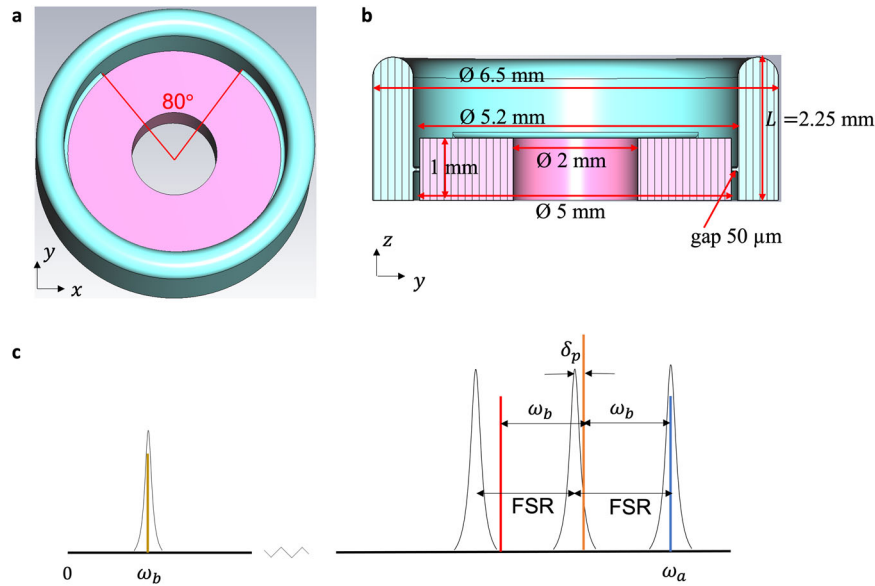


**Fig. 1 Three-dimensional superconducting RF (SRF) cavity and electro-optic design for quantum transduction.** **a** Top view of the SRF cavity enclosing a bulk lithium niobate (LN) optical resonator (pink). The cyan region refers to the vacuum volume enclosed by the niobium (Nb) (not visible). The LN resonator has a hole (grey) in the center with a 2 mm diameter which is filled with Nb. **b** Side view of the cross-section of the RF cavity with the enclosed LN resonator.  $L$  is the length of the stub, which is used to tune the resonant frequency. **c** Diagram of the three-wave mixing process for microwave-optical quantum transduction. The optical pump is injected into the optical resonator. The pump is detuned by  $\delta_p$  from the central optical mode. Mixing of the optical pump and the weak microwave signal at frequency  $\omega_b$  generates two optical sidebands (red and blue). The blue sideband signal excites the optical mode at  $\omega_a$ , whereas the red sideband signal is off-resonance and inhibited. Reversely, by mixing the optical pump and the optical signal at  $\omega_a$ , microwave photons at  $\omega_b$  are coherently generated. Thereby, this scheme enables bidirectional conversion between the microwave field at  $\omega_b$  and the optical field at  $\omega_a$ .

optical field in the LN crystal structure and the microwave field. Through simulations, we study and optimize the optical coupling strength between the prism coupler and the optical resonator. We demonstrate through simulations that our system can achieve 50% quantum transduction efficiency at 140  $\mu\text{W}$  pump power, with an operating bandwidth of 100 kHz. Furthermore, with a superconducting qubit coupled to the microwave cavity, the transducer can read out the quantum state of the qubit with high resolution of the dispersive shift. Finally, such transducer devices can be exploited for high-fidelity heralded quantum entanglement generation between two distant quantum processing units, as well as for high-precision microwave signal measurement and quantum sensing.

## RESULTS

### Device design

The proposed system consists of an LN whispering gallery mode (WGM) optical resonator enclosed by a 3D bulk niobium superconducting RF cavity (Fig. 1a). The LN resonator with a 5 mm diameter is made of a disk with the central part removed and has the crystal axis in the  $z$  direction ( $z$ -cut), aligned to the electric field distribution. The electric field is enhanced by defining two symmetric interaction sections with a narrow vertical vacuum gap of 50  $\mu\text{m}$  spanning 80° in the azimuthal direction (Fig. 1b). Such a design reshapes the electric field distribution. It enables the concentration of the microwave field onto the region near the rim of the LN disk where the WGM is located. This is the key to enhancing the interaction between the microwave and optical modes<sup>44</sup>. It is noted that previous designs relied on electrode deposition to concentrate the microwave field onto the WGM region near the rim of the LN crystal. Such an approach requires more complicated fabrication techniques, including metal evaporation and photolithography, which could introduce additional optical losses to the WGM. In contrast, our design is mainly based on engineering the geometry of the SRF cavity and the embedded

LN crystal. The region outside the thin 80° vacuum gap allows for the placement of an optical coupler, such as a diamond prism, which will be discussed further.

Bulk Nb SRF cavities are attractive for quantum applications because of the high electromagnetic field energy in the large mode volume. SRF cavities built for particle accelerators have demonstrated  $E_{\text{max}} = 10 \text{ MV} \cdot \text{m}^{-1}$ , with  $Q > 10^{10}$ <sup>40</sup>. In transduction, the high field density within the cavity enhances the light-matter interactions and, thus, the electro-optic effect.

The LN crystal enclosed in the SRF cavity occupies most of the volume, with a participation ratio ( $p$ ) in the order of 0.925, i.e., 92.5% of the microwave volume is occupied by the LN crystal. The participation ratio is defined as:

$$p = \frac{\int_{V_d} \epsilon_d |E|^2 dV_d}{\int_V \epsilon_0 |E|^2 dV}, \quad (1)$$

where  $E$  is the electrical field,  $V$  is the total volume, and  $V_d$  is the volume of the dielectric crystal.  $\epsilon_{d,0}$  are the dielectric permittivities of the dielectric LN crystal and vacuum, respectively. The microwave quality factor at cryogenic temperatures is mainly determined by the losses in the dielectric crystal, which include several sources of losses, such as the two-level-system (TLS) loss of impurities in the LN crystal, the piezo-electric loss, the thermal quasiparticle loss, and others<sup>45</sup>. For simplicity, we use a single value of loss tangent ( $\tan \delta$ ), including all channels of losses in our evaluation, which has been reported to be in the order of  $10^{-5}$  at cryogenic temperatures<sup>46</sup>. The quality factor is the ratio between the energy stored in the cavity ( $U$ ) and the dissipated power ( $P_{\text{loss}}$ ), i.e.,

$$Q = \frac{\omega_b U}{P_{\text{loss}}} = \frac{\omega_b \mu_0 \int_V |H|^2 dV}{\int_S |H|^2 dS}, \quad (2)$$

where  $H$  is the magnetic field and  $\omega_b$  is the resonant frequency of the RF cavity. The total loss rate ( $\gamma_b$ ) of the RF cavity is determined by the coupling losses of the input and output couplers ( $\gamma_{b,c}$ ), the

intrinsic  $Q$  of the RF cavity ( $Q_0$ ), and the dielectric quality factor ( $Q_d$ ):

$$\frac{Y_b}{\omega_b} = \frac{Y_{b,c}}{\omega_b} + \frac{1}{Q_0} + \frac{1}{Q_d}, \quad (3)$$

where the dielectric quality factor is inversely proportional to the loss tangent:

$$p \times \tan \delta = \frac{1}{Q_d}. \quad (4)$$

With a high participation ratio, the dominant source of microwave loss is the dielectric loss, which is determined by the loss tangent of the electro-optic material. If  $Q_0$  is higher than  $Q_d$ , the bare microwave loss on the cavity wall is negligible. Such a requirement is satisfied by superconducting materials such as niobium (Nb) and aluminum (Al) (see Methods). The choice of cavity materials is further discussed in Supplementary Note 1.

To find the optimal parameters of the RF cavity geometry for electro-optic interactions, a trade-off exists between the microwave quality factor, which is reduced by the large dielectric participation ratio, and the maximum electric field in the volume of WGM near the rim of the LN resonator, which is enhanced by more dielectric participation. In our design, as the microwave volume is essentially reduced to the volume of the crystal, the losses are mostly concentrated in the dielectric LN resonator, which defines the internal quality factor of the microwave cavity. The resonant frequency is tunable by adjusting the length of the lateral stub (see Supplementary Note 2).

### Model of the system

The electro-optic quantum transduction is based on a three-wave mixing nonlinear process between the optical pump, the optical signal, and the microwave signal (Fig. 1c). An optical mode  $a_p$  at frequency  $\omega_p$  is pumped by the coherent light, enabling the coupling and bidirectional conversion between the other optical mode ( $a$ ) at frequency  $\omega_a$  and a microwave mode ( $b$ ) at  $\omega_b$ . To satisfy the energy conservation while avoiding the Stokes photon generation into the undesired optical mode, the free spectral range (FSR) of the WGMs, i.e., the frequency difference between two WGMs with consecutive azimuthal mode numbers is chosen to be slightly larger than the microwave resonance frequency ( $\omega_b$ ). Hence the Hamiltonian of the system is given by<sup>31</sup>

$$H = \hbar\omega_p a_p^\dagger a_p + \hbar\omega_a a^\dagger a + \hbar\omega_b b^\dagger b - \hbar g_{eo} (b + b^\dagger)(a_p + a). \quad (5)$$

The single-photon electro-optic coupling strength ( $g_{eo}$ ) is determined by the field overlap between the microwave mode and the WGM:

$$g_{eo} = n^2 r_{33} \sqrt{\frac{\hbar\omega_p \omega_a \omega_b}{8\epsilon_0 \epsilon_b V_p V_a V_b}} \int_V \psi_a^* \psi_p \psi_b(r, \theta, \phi) dV, \quad (6)$$

where  $n$  is the extraordinary refractive index of LN near 1550 nm,  $r_{33}$  is the linear electro-optic coefficient;  $V_i$  ( $i = p, a, b$ ) are the mode volumes of the mode  $i$  with the dielectric constant  $\epsilon_i$ , the frequency  $\omega_i$  and the single-photon electric field  $E_i(r, \theta, \phi) = \sqrt{\hbar\omega_i/2\epsilon_0\epsilon_i V_i} \psi_i(r, \theta, \phi)$ .

As the pump and signal optical modes have a mode number difference of 1, their amplitudes can be expressed as  $\psi_p = \phi_p(r, \theta) e^{-im\phi}$  and  $\psi_a = \phi_a(r, \theta) e^{-i(m+1)\phi}$ . To satisfy the momentum conservation, a dipole mode is chosen for the microwave cavity whose electric field oscillates along the azimuthal direction as  $E_{RF}(r = R_0, \theta = 0, \phi) = \tilde{E}_{RF}(\phi) \cos(\phi)$ , where  $\tilde{E}_{RF}(\phi)$  is the correction function that maps the sinusoidal function to the realistic mode distribution. Since the mode size of the WGM is relatively small, we can assume that the microwave electric field has uniform  $r$  and  $\theta$  distribution inside the WGM volume<sup>37</sup>, and

therefore, calculate  $g_{eo}$  as

$$g_{eo} = \frac{1}{16\pi} n^2 r_{33} \sqrt{\omega_p \omega_a} \sqrt{\frac{\hbar\omega_b}{W}} \int_0^{2\pi} \tilde{E}_{RF}(\phi) d\phi, \quad (7)$$

where the electric field is normalized by the photon number determined by the total stored microwave energy ( $W$ ) in the RF cavity. As seen from Eq. (7), maximizing the electric field ( $\tilde{E}_{RF}$ ) by tailoring the microwave mode distribution is essential to obtain a large electro-optic coupling rate.

To trigger the three-wave mixing process efficiently, a strong coherent pump with frequency  $\omega_a - \omega_b$  and detuned from  $\omega_p$  by  $\delta_p = FSR - \omega_b$  is coupled to the optical resonator (Fig. 1c). The Hamiltonian in the rotating-wave approximation is reduced to

$$H = \hbar\omega_p a_p^\dagger a_p + \hbar\omega_a a^\dagger a + \hbar\omega_b b^\dagger b - \hbar g_{eo} (\alpha^* a b^\dagger + a a^\dagger b), \quad (8)$$

where  $a$  is the amplitude of the pump field in the optical cavity.

Assuming an optical driving field  $A_{in} e^{-i(\omega_a + \Delta)t}$  and a microwave driving field  $B_{in} e^{-i(\omega_b + \Delta)t}$  are applied as the signals for conversion, the dynamics of the system are given by

$$\frac{da}{dt} = (-i\omega_a - \frac{\gamma_a}{2})a + ig_{eo}ab - \sqrt{\gamma_{a,c}} A_{in} e^{-i(\omega_a + \Delta)t}, \quad (9)$$

$$\frac{db}{dt} = (-i\omega_b - \frac{\gamma_b}{2})b + ig_{eo}\alpha^* a - \sqrt{\gamma_{b,c}} B_{in} e^{-i(\omega_b + \Delta)t}, \quad (10)$$

with

$$\alpha = \frac{\sqrt{\gamma_{a,c}} A_{in}}{i\delta_p - \frac{\gamma_a}{2}}, \quad (11)$$

where, for a generic  $m$  mode ( $m = a, b$ ),  $\gamma_m$  is the total loss rate, consisting of both the internal loss and external (coupling) loss:  $\gamma_m = \gamma_{m,0} + \gamma_{m,c}$ . By solving the system's dynamics in the steady state, we can obtain the transfer functions for conversion from the microwave to optical signals and vice versa, which are equal due to reciprocity. The bi-directional frequency conversion efficiency depends on the microwave-optical cooperativity and losses:

$$\eta = \frac{\gamma_{a,c} \gamma_{b,c}}{\gamma_a \gamma_b} \times \frac{4C}{(1+C)^2}, \quad C = \frac{4n_p g_{eo}^2}{\gamma_a \gamma_b}, \quad (12)$$

where  $C$  is the cooperativity between the optical and the microwave modes, which depends on the photon number in the pump mode ( $n_p$ ). The second term of Eq. (12) is the internal efficiency:  $\eta_i = 4C/(1+C)^2$ , which reaches unity at  $C = 1$ .

As a result, the limiting factors in the attainment of high efficiency in microwave-optical transduction are:

- The quality factor of the microwave hybrid cavity ( $Q_b$ ) – While the optical  $Q_a$  can reach  $10^7$ , microwave  $Q_b$  is limited in the state-of-art schemes.
- The single-photon electro-optic coupling coefficient ( $g_{eo}$ ) – This parameter is determined by the overlap between microwave and optical fields and has a trade-off with the microwave  $Q$  factor.
- The pump power – High pump power leads to overheating of the device, and thermal quasiparticle poisoning, which hinders the device's operation in the quantum regime.

### Simulation of the microwave and optical modes

Using the Finite-Difference Time-Domain (FDTD) method, we simulate the electric field distribution of a 9 GHz dipole mode in the RF cavity with the LN resonator embedded (Fig. 2a, b). As noted, the electric field has a strong concentration around the rim of the LN crystal. The dipole mode property is verified by the complete oscillation of the electric field along the rim of the disk (Fig. 2c). The field distribution is distorted from a standard sinusoidal shape due to the variation in the distance between the RF cavity wall and the LN resonator. The proper choice of the size

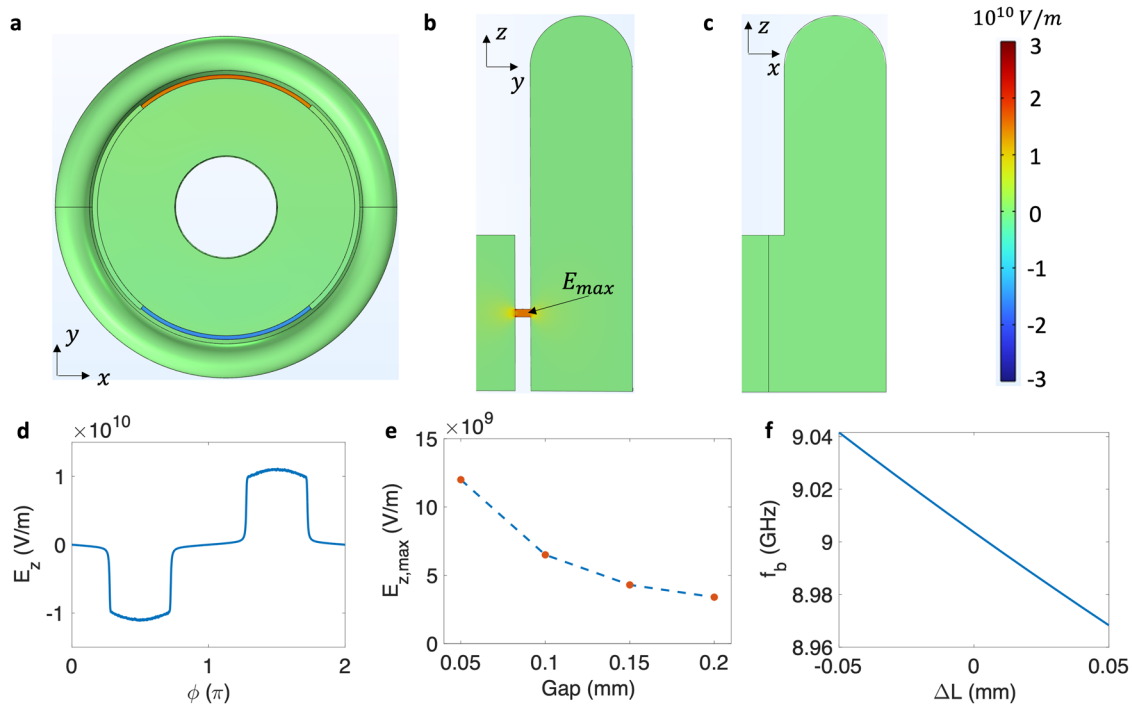


**Fig. 2 Simulation of the microwave mode near 9 GHz.** The simulation is based on stored energy of 1 J. **a–c**  $z$ -component of the electric field in the SRF cavity on the **(a)**  $x - y$  plane, **(b)**  $y - z$  plane, and **(c)**  $x - z$  plane. The prism for the optical coupling is located in the wider section displayed in **c**. **d** Azimuthal distribution of the  $z$  component of the electric field ( $E_z$ ) along the rim of the LN optical resonator. **e** Maximum electric field on the  $y - z$  plane at the rim of the LN crystal (shown in **b**) versus the gap size (shown in Fig. 1**b**). **f** Microwave frequency tuning as a function of variations of the vacuum stub length  $\Delta L$ .

of the narrow gap between Nb walls is critical for the optimization of the field magnitude on the rim of the LN crystal (Fig. 2d). The maximum  $z$  component of the electric field is over  $1 \times 10^{10} \text{ V} \cdot \text{m}^{-1}$ , yielding a single-photon electro-optic coupling coefficient of  $2\pi \times 46.75 \text{ Hz}$  based on Eq. (7).

As noted before, due to the extremely low niobium loss and high intrinsic  $Q$  for the RF cavity, the microwave loss at cryogenic temperature is dominated by the loss tangent of LN crystals. Based on the reported LN loss tangent ( $\tan \delta \sim 1 \times 10^{-5}$ )<sup>47</sup>, we estimate the quality factor of the microwave dipole mode to be  $1.1 \times 10^5$ , which is well above what was achieved in previous works. The removal of the central part of the disk allows for lower microwave losses on the redundant LN crystals where the WGM does not exist. While further optimization is possible by further enlarging the diameter of the central hole, the proposed design, with an inner diameter of 2 mm, is the trade-off solution between the fabrication techniques, the microwave losses, and the optimal overlap between microwave and optical modes. To ensure that the FSR matches the microwave resonance frequency ( $\omega_b$ ), we tune  $\omega_b$  by applying a deformation to the volume of the stub  $L$  (Fig. 2f). The sensitivity of  $700 \text{ MHz} \cdot \text{mm}^{-1}$  allows the tunability of the cavity resonant frequency by several tens of MHz and with high resolution through piezo stages. Additional details of the microwave design are available in Supplementary Note 2.

We also simulate the mode distribution of an optical WGM with a frequency around 192.43 THz by the FDTD approach (Fig. 3b). Based on the eigenfrequencies of three WGMs with consecutive mode numbers, we found that the FSR is around 8.93 GHz. The curvature of the side wall is 2.5 mm, making it appear near-flat. The smooth surface enabled with state-of-the-art LN fabrication techniques can ensure a high optical quality factor ( $Q_a$ ) above  $10^7$ . In addition, the upper and bottom surfaces can also be engineered to be slightly rounded depending on fabrication needs. Those minor curvatures will have negligible influence on the microwave and optical mode profile.

To couple the optical pump into the WGM, a high-index prism is placed close to the rim of the optical resonator (Fig. 3a). The effect of the prism and the apertures to couple the beam light to the optical resonator is negligible on the microwave loss, as discussed in Supplementary Note 3. The coupling strength between the resonator and the prism ( $\gamma_{a,c}$ ) is controlled by their spatial gap. It is known that the pump photon number always reaches the maximum at critical coupling<sup>48</sup>, i.e.,  $\gamma_{a,c}$  is equal to the intrinsic loss rate  $\gamma_{a,0}$  (Fig. 3c). However, the critical coupling does not lead to optimized transduction efficiency. As shown in Fig. 3d, the cooperativity is maximized around  $\gamma_{a,c} = 0.7 \times \gamma_{a,0}$ , regardless of the microwave quality factor ( $Q_b$ ). The overall transduction efficiency, however, is optimized at different values of coupling losses for various microwave quality factors ( $Q_b$ ) (Fig. 3e). In our case, i.e.,  $Q_b \sim 10^5$ , the optimized coupling loss is around  $\gamma_{a,c} = 2.3 \times \gamma_{a,0}$ . This lightly overcoupled regime is favorable for efficient readout of the transduction signal.

### Figures of merit of the quantum transducer

With the device design presented above, we explore the figures of merit of the transduction process at different conditions of operation. In particular, a high-performance transducer should have: (1) high cooperativity and efficiency; (2) low operating pump power, which indicates low thermal noise; and (3) large bandwidth for signal conversion.

As noted, a high level of optical pump benefits the cooperativity and transduction efficiency but introduces more overheating of the device, leading to excessive thermal noise photons. Moreover, the stray infrared pump photons that are scattered out of the designed optical path and illuminate on the RF cavity surface can break the Cooper pairs of the Nb and deteriorate the coherence of RF cavities and qubits<sup>49,50</sup>. To enable a quantum operation, as shown by previous literature, the pump power needs to be in the sub-mW level<sup>37</sup>, while the exact noise photon level depends on

the specific geometry and the materials of the physical systems<sup>36</sup>. Therefore, we study the cooperativity and transduction efficiency as a function of the pump power for our design. We compare the cases with different microwave quality factors and find that the conversion efficiency is greatly enhanced by a high microwave quality factor ( $Q_b$ ). Our design can achieve 0.58 cooperativity and 50% conversion efficiency at 140  $\mu\text{W}$  pump power (Fig. 4a and b). This level of performance greatly exceeds the limit of state-of-art technology. Current transduction designs with lower  $Q_b$  rely on  $\sim\text{mW}$  pump power to achieve less than 0.1 cooperativity and 2% conversion efficiency<sup>7</sup>.

Moreover, we investigate the bandwidth of the transducer by assuming that the RF cavity is probed by a weak microwave signal with a certain frequency detuning ( $\Delta$ ) from the operating frequency  $\omega_b$ . From the simulation, we find out that the bandwidth is enhanced by decreasing  $Q_b$  (Fig. 4c). This is due to

the fact that a larger linewidth of the microwave mode can tolerate a wider frequency range of the input signal. Therefore, there is always a trade-off between the transduction efficiency and the operating bandwidth. For our design, with  $Q_b \sim 10^5$ , the microwave bandwidth ( $\Delta_b$ ) is 100 kHz, with the center of the spectrum window located at  $\omega_b$ .

The figures of merit for this design are summarized in Table 1.

### Quantum transduction in a hybrid quantum electrodynamics system

We now extend the electro-optic quantum transducer to a cavity QED system where the RF cavity is dispersively coupled to a superconducting transmon qubit located within the cavity mode volume. With the hybrid QED system built upon our transducer, one can convert the microwave input signal to optical photons, and also optically read out the qubit quantum state via optical

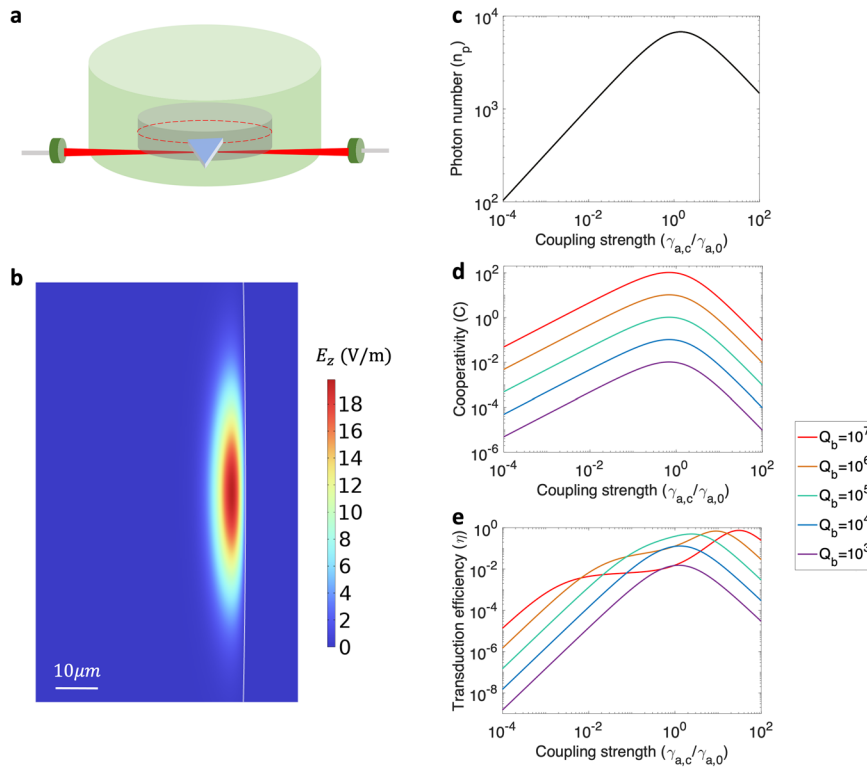


**Fig. 3 Optical design for quantum transduction.** **a** Schematic diagram of the optical coupling scheme with a prism coupler. The optical pump and signal are focused onto the prism coupler via a microlens. The reflected light is collected by another microlens. **b** Whispering gallery mode in the LN optical resonator. The white lines show the boundary of the LN resonator. **c** Photon number in the pump mode versus the coupling strength between the prism and the optical resonator ( $\gamma_{a,c}$  normalized by the intrinsic optical loss rate  $\gamma_{a,0}$ ). **d** Cooperativity and **e** transduction efficiency versus the resonator-prism coupling for different quality factors of the microwave cavity ( $Q_b$ ). Parameters:  $Q_a = 10^7$ ,  $Q_b = 10^5$ ,  $\gamma_{b,c} = 3.4 \times \gamma_{b,0}$ ,  $g_{eo} = 2\pi \times 46.75$  Hz,  $\delta_p = 10$  MHz.

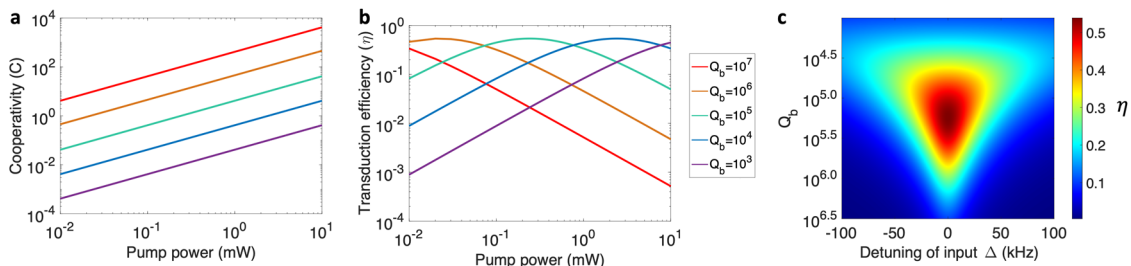


**Fig. 4 Figures of merit of the transduction process.** Effect of the incoming pump power on the **(a)** cooperativity and the **(b)** transduction efficiency ( $\eta$ ) for different values of microwave quality factors ( $Q_b$ ). **c** Transduction efficiency as a function of  $Q_b$  (in the logarithmic scale) and the frequency detuning of the optical/microwave input ( $\Delta$ , in the linear scale). The parameters are the same as in Fig. 3.

measurement<sup>51</sup>. The full Hamiltonian of the hybrid QED system is given as

$$H = \frac{1}{2} \hbar \omega'_q \sigma_z + \hbar \omega_a a^\dagger a + \hbar \omega'_b b^\dagger b - \hbar g_{eo} (a^* a b^\dagger + a a^\dagger b) + \hbar \chi b^\dagger b \sigma_z, \quad (13)$$

where  $\omega'_{q,b}$  refer to the renormalized frequencies of the qubit and the microwave cavity mode, and  $\chi$  is the dispersive coupling rate. As indicated by the term  $\hbar(\omega'_b + \chi \sigma_z) b^\dagger b$ , the excited state of the qubit induces a dispersive shift ( $\chi$ ) to the resonance frequency of the RF cavity. Conventionally, the qubit state can be measured by characterizing the frequency shift in the spectrum of the readout cavity. Based on our design, the dispersive frequency shift can be further converted to the amplitude change of the optical signal as the readout of the transducer. Thus, the optical readout and transfer of the state information of the superconducting qubit can be achieved<sup>51</sup>.

We assume that the renormalized RF resonance frequency  $\omega'_b$  is equal to  $FSR - \delta_p$ , and a weak microwave readout pulse with amplitude  $B_{in}$  and frequency  $\omega = \omega'_b$  is added to the RF cavity. The dynamics of the system in the interaction picture are given by

$$\frac{d\tilde{a}}{dt} = (i\chi - \frac{\gamma_a}{2})\tilde{a} + ig_{eo}a\tilde{b}, \quad (14)$$

$$\frac{d\tilde{b}}{dt} = -\frac{\gamma_b}{2}\tilde{b} + ig_{eo}a^*\tilde{a} - \sqrt{\gamma_{b,c}}B_{in}e^{i\chi t}, \quad (15)$$

where we define  $a = \tilde{a}e^{-i(\omega_a + \chi)t}$  and  $b = \tilde{b}e^{-i(\omega'_b + \chi)t}$ . The resulting frequency components of the output optical field of the hybrid QED system are shown in Fig. 5a.

Based on the above analysis and our design parameters, we simulate the transduction efficiency, which determines the level of

optical output, as a function of the dispersive shift  $\chi$  (Fig. 5b). The transduction efficiency shows quick decay as the magnitude of the dispersive shift increases. This is mainly due to the fact that, when the microwave frequency is detuned from both the optical FSR and the readout pulse, the three-wave mixing process becomes increasingly less efficient. As the  $Q_b$  increases, the resolution to distinguish the dispersive shift becomes higher, which can reduce the error rate in the qubit state readout.

Figures 4c and 5b show similar behaviors that lead to a trade-off between the input detuning bandwidths and the dispersive shift resolution. At  $Q_b = 10^5$ , we find that our system can tolerate  $\pm 50$  kHz detuning for the input signal around the RF resonance frequency while being able to fully resolve  $\pm 98$  kHz ( $\eta < 0.1$ ) dispersive shift induced by the qubit. With typical superconducting qubit-cavity coupling strength up to  $\sim$  MHz level<sup>52</sup>, this scheme can therefore work for a variety of QED systems to optically read out qubit information and connect superconducting qubits in remote quantum processors<sup>51</sup>.

For successful dispersive measurements, the readout rate should be much faster than the decay of the qubit state. The lifetime of state-of-the-art transmon qubits ( $T_1$ ) is at a level of  $100 \mu\text{s}$ <sup>53</sup>. The transduction readout process occurs at a rate of  $\max(\frac{1}{g_{eo}|a|}, \frac{1}{\gamma_{a,c}}) \sim 3 \mu\text{s} < T_1$ . Further improving the efficiency of the transducer can lead to a higher signal-to-noise ratio and fidelity in qubit readout<sup>3</sup>.

### Heralded entanglement generation based on transducers

We discuss an application of our high-efficiency quantum transducer to quantum entanglement generation. One of the key challenges for realizing quantum networks is creating entangled quantum states between two distant quantum nodes. It has been proposed that the optically heralded quantum entanglement can be generated with high-efficiency quantum transducers<sup>54,55</sup>. Such a scheme can work in both the regimes of blue sideband pumping and red sideband pumping, with the latter offering higher fidelity due to its protection against multiphoton generation.

Here, we analyze the entanglement generation features based on the optically heralded approach using our electro-optic transducer. The setup consists of two quantum transducers spatially separated. The optical cavities of the transducers are coupled to optical waveguides, i.e., fiber optics, which send the generated optical photons to a beam splitter followed by two detectors without distinguishing which-path information. The heralded signal indicates the generation of remote entangled microwave photon pairs in superconducting cavities. In entanglement generation, the target state is a state in the two distant microwave cavities  $|\psi\rangle = c_1|01\rangle + c_2|10\rangle$ . Such a state can be generated by either the blue-sideband pumping or red-sideband pumping approach, as discussed below.

**Table 1.** Main design parameters and figures of merit for the presented 3D transduction device based on the coupling of an SRF cavity and an electro-optic resonator.

Parameter	Symbol	Unit	Value
Free spectral range	FSR	GHz	8.93
Loss tangent	$\tan \delta$		$1 \times 10^{-5}$
Optical quality factor	$Q_a$		$1 \times 10^7$
Microwave quality factor	$Q_b$		$1.1 \times 10^5$
Single-photon electro-optic coupling rate	$g_{eo}/2\pi$	Hz	46.75
Pump frequency detuning	$\delta_p$	MHz	10
Pump power	$P_p$	$\mu\text{W}$	140
Cooperativity	C		0.58
Conversion efficiency	$\eta$	%	50
Microwave bandwidth	$\Delta_b$	kHz	100

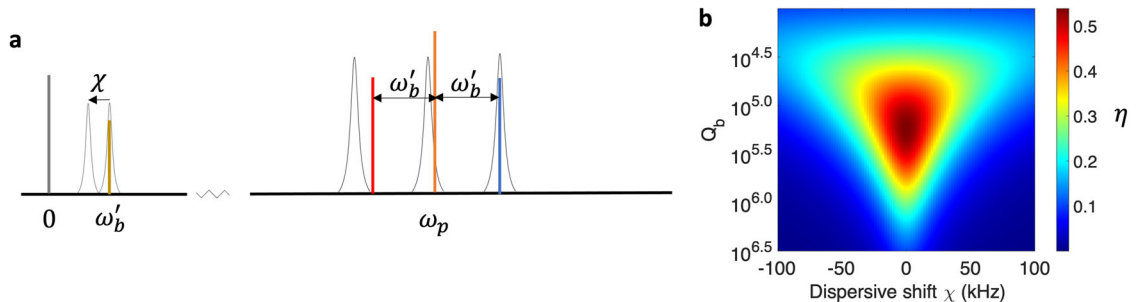


**Fig. 5** Transduction in a superconducting QED system with a qubit. **a** Frequency spectrum for the output signal of the quantum transducer. **b** Conversion efficiency ( $\eta$ ) as a function of the microwave quality factor ( $Q_b$ , in the logarithmic scale) and the dispersive shift of the microwave resonance frequency induced by the qubit ( $\chi$ , in the linear scale).

As for the blue-sideband pumping case, a pump optical photon can be converted into a microwave and an optical photon. The photon generation in one transducer follows a Poissonian process with a photon generation rate  $r_0$ . Therefore, the probability that a photon is generated in each microwave cavity is expressed as

$$P_1 = r_0 \Delta t e^{-r_0 \Delta t}, \quad (16)$$

while, on the other hand, the probability that no photon is generated is

$$P_0 = e^{-r_0 \Delta t}. \quad (17)$$

Therefore, the probability that one photon is generated in each microwave cavity is given as

$$P_{11} = P_1^2. \quad (18)$$

Furthermore, there is a possibility that more than one photon is generated in one microwave cavity. The probability associated with this event is

$$P_{m > 1, n \leq 1} = P_{m \leq 1, n > 1} = (1 - P_0 - P_1)(P_0 + P_1). \quad (19)$$

Moreover, there can also be more than one photons generated in both cavities, with the probability

$$P_{m > 1, n > 1} = (1 - P_0 - P_1)^2. \quad (20)$$

One can write the final state of the system as a superposition of two-photon Fock states:

$$\begin{aligned} |\psi_f\rangle = & \sqrt{P_{00}}|00\rangle + \sqrt{P_{10}}|10\rangle + \sqrt{P_{01}}|01\rangle + \sqrt{P_{11}}|11\rangle \\ & + \sqrt{P_{m > 1, n \leq 1}}|m > 1, n \leq 1\rangle \\ & + \sqrt{P_{m \leq 1, n > 1}}|m \leq 1, n > 1\rangle \\ & + \sqrt{P_{m > 1, n > 1}}|m > 1, n > 1\rangle, \end{aligned} \quad (21)$$

where we neglect the phase information in the coefficients. Assuming fixed duration time ( $\Delta t$ ) of the transduction process, the entangled microwave photon pair is generated at a rate  $2r_0 e^{-r_0 \Delta t} \frac{\Delta t}{\Delta t + t_r}$ , where  $t_r$  is the microwave reset time after each generation event<sup>55</sup>. The infidelity corresponds to the probability that each microwave cavity contains one photon, or that more than one photon is generated in at least one cavity. Therefore, the fidelity is expressed as

$$\eta_b = \frac{P_{10} + P_{01}}{P_{10} + P_{01} + P_{11} + P_{m > 1, n \leq 1} + P_{m \leq 1, n > 1} + P_{m > 1, n > 1}}. \quad (22)$$

In the red-sideband pumping case, the remote entanglement is enabled by first preparing both microwave cavities at the one-photon state while leaving the optical cavity at the zero-photon state<sup>56,57</sup>. Upon the simultaneous onset of the transduction processes in both transducers, a microwave photon can be

converted to an optical photon that triggers the “click” of the detector, with the probability

$$P_1 = 1 - \exp(-r_0 \Delta t). \quad (23)$$

As such, the probability that no optical photon is generated is instead given by

$$P_0 = \exp(-r_0 \Delta t). \quad (24)$$

As there cannot be more than one photon generated in a microwave cavity, the generated state of the whole system, including two quantum units, is simply  $|\psi_f\rangle = \sqrt{P_{00}}|00\rangle + \sqrt{P_{10}}|10\rangle + \sqrt{P_{01}}|01\rangle + \sqrt{P_{11}}|11\rangle$ . Moreover, the infidelity is only affected by  $P_{11} = P_1^2$ , which leads to

$$\eta_r = \frac{P_{10} + P_{01}}{P_{11} + P_{10} + P_{01}}. \quad (25)$$

Here, we analyze the rate and infidelity of entanglement generation based on the parameters in our design of the transducers. While the entanglement generation rate is optimized at a pump power higher than 1 mW, the increase in pump power reduces the fidelity, due to the additional possibility of generating more than one microwave photon (Fig. 6). This trade-off limits the amount of pump power that can be applied, as well as the speed of entangled state generation for distributed quantum communication. For our design, a 20 kHz entanglement rate can be realized at a pump power of 18  $\mu$ W with an infidelity of about 0.01.

### Enhanced quantum sensing with high-coherence transduction devices

The high-efficiency microwave-optical transducer can also enhance the measurement precision of weak microwave signals in quantum sensors. The microwave signal measurement is of critical importance in various fundamental studies and applications, including, for instance, single photon detection, highly sensitive axion and dark photon haloscope measurement, new physics particle searches in the THz range, and so on<sup>42</sup>. In the up-conversion operation performed with this hybrid transduction system, the microwave information is converted to the optical regime through self-heterodyne techniques, which have the advantage of eliminating the local oscillator (LO) used in conventional super-heterodyne mixers, reducing, therefore, complexity, power consumption, pump power, and thermal quasiparticle poisoning.

One issue associated with the transducer working for precise measurement is that the conversion process introduces additional single-photon shot noise and back-action noise. The standard noise spectrum of microwave detection using single-quadrature

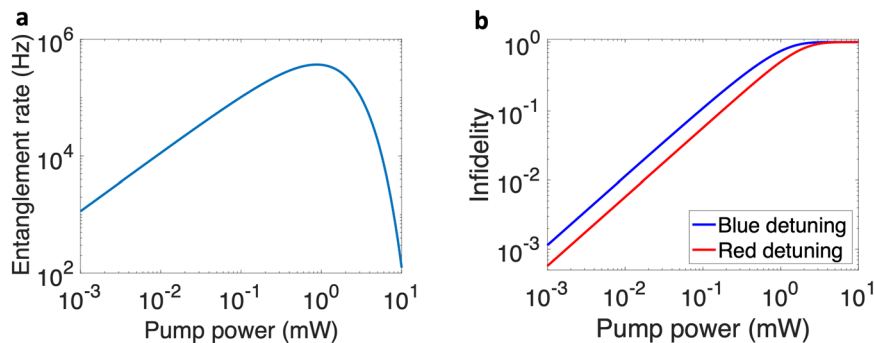


**Fig. 6** Optically heralded entanglement generation based on electro-optic quantum transducers. **a**, **b** Entanglement generation rate (**a**) and infidelity (**b**) as a function of pump power. Microwave reset time  $t_r = 1 \mu$ s. Duration time  $\Delta t = 1 \mu$ s.

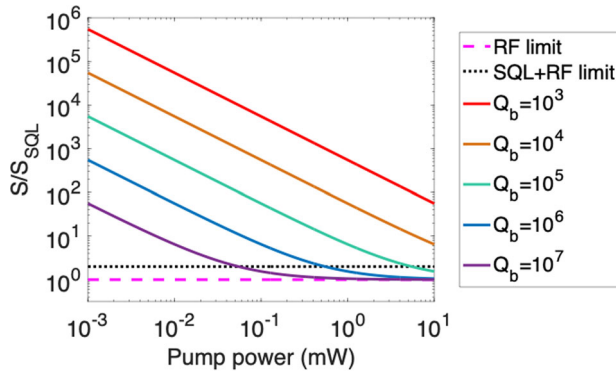


**Fig. 7 High-efficiency transducer for high-precision microwave measurement.** Noise spectral density ( $S$ ) normalized by the standard quantum limit (SQL) as a function of the pump power, with back-action noise cancellation. The parameters follow our transducer design, except that the optical Q factor is chosen to be  $10^8$ .

measurement is given by:

$$S(\Delta) = 2\kappa_b(2n_T + 1) + \frac{(\kappa_b^2 + \Delta^2)(\kappa_a^2 + \Delta^2)}{4n_p g_{eo}^2} + \frac{4n_p g_{eo}^2}{\kappa_a^2 + \Delta^2}, \quad (26)$$

which is ultimately limited by both the standard quantum limit (SQL) and the RF noise floor as  $S(\Delta) \geq S_{RF} + S_{SQL}$ , where  $S_{RF} = 2\kappa_b(2n_T + 1)$  and  $S_{SQL} = \sqrt{\kappa_b^2 + \Delta^2}$ .

The enhancement of microwave photons measurement at the quantum threshold through transduction methods and with the assistance of back-action noise cancellation techniques have been reported in ref. <sup>58</sup>. In particular, a judicious choice of combination of independent quadrature measurements can lead to the cancellation of the back-action noise in the transduction process<sup>58</sup>. In the back-action evading approach, the detection noise density is rather given by:

$$S(\Delta) = 2\kappa_b(2n_T + 1) + \frac{(\kappa_b^2 + \Delta^2)(\kappa_a^2 + \Delta^2)}{C\kappa_a\kappa_b}, \quad (27)$$

where  $n_T$  is the number of thermally excited photons and  $C$  is the cooperativity for transduction following Eq. (12). Therefore, with the back-action scheme, there is a possibility to break the standard detection limit with reference to the SQL. Figure 7 shows the noise spectral densities as a function of pump power for different microwave Q's. The noise level of the sensor can be lowered down to the RF limit breaking the SQL limit by increasing the microwave coherence time or increasing the pump power. Notably, the large cavity coherence can significantly reduce the required pump power to obtain a high precision for detection, making it meaningful to increase the coherence time of cavities further.

## DISCUSSION

We design a three-dimensional electro-optic system for high-efficiency and low-pump-power microwave-optical quantum transduction based on SRF technology. The transduction process is optimized by calculating the figures of merit versus various degrees of freedom in the SRF cavity geometry, LN crystal geometry, optical coupling, and optical pump power. Through microwave and optical analysis and simulations, we show transduction performance and up to 50% frequency conversion at very low pump power. This level of efficiency is critical for achieving frequency conversion with meaningful capacity in the quantum regime<sup>59</sup>. Compared to the previous works, this design overcomes the conventional challenge of achieving high transduction efficiency and low incoming pump power simultaneously.

This platform holds great potential for the near-future realization of several applications. The electro-optic quantum transducer allows for optical readout of quantum information in superconducting QED systems inside the dilution refrigerators<sup>60</sup>. It provides a critical interface for achieving huge scaling capabilities for quantum computers, going beyond the limit of local dilution refrigerators, building links between superconducting quantum processors, and realizing remote entanglement over optical fibers.

High conversion efficiency can also be leveraged in quantum sensing techniques breaking the standard quantum limit (SQL) by applying back-action evading schemes or squeezing techniques for the detection of microwave photons. Thus, these transduction techniques can serve as a platform for fundamental physics experiments such as dark matter detection over a wide frequency range.

## METHODS

### Material requirement for the microwave cavity

In our design, the LN crystal has a filling factor above 90%, and the LN loss tangent at cryogenic temperatures is  $Q_d \sim \tan \delta = 10^{-5}$ <sup>46</sup>. Therefore, the quality factor associated with the properties of the dielectric part is  $Q_d \sim 10^5$ . The intrinsic quality factor of the bare cavity without LN crystal ( $Q_0$ ) should be at least in the order of  $10^6$  to avoid additional microwave losses and make a minimal impact on the total  $Q_b$ . Such a requirement is satisfied by superconducting materials, such as niobium or aluminum. However, it is not easily satisfied by a normal conducting metal with higher losses (see Supplementary Note 1). Among superconducting materials, niobium is preferable to aluminum, as the critical temperature in aluminum is lower than in niobium.

### RF design

Electromagnetic (EM) simulations are performed using commercially available CST Studio Suite and COMSOL Multiphysics software packages. The RF design is optimized to achieve a high electric field on the rim of the LN resonator and, therefore, a significant interaction with the optical field. Results from EM simulations are used to model the quantum transducer and to compute the figures of merit, such as the single-photon electro-optic coupling coefficient, the cooperativity, and the transduction efficiency. Furthermore, the parameters derived from the simulations are applied to qubit readout in QED systems, heralded entanglement generation, and quantum sensing.

### DATA AVAILABILITY

The numerical data generated in this work is available from the authors upon reasonable request.

### CODE AVAILABILITY

The code generated in this work is available from the authors upon reasonable request.

Received: 30 June 2022; Accepted: 2 December 2022;

Published online: 21 December 2022

## REFERENCES

- Schoelkopf, R. & Girvin, S. Wiring up quantum systems. *Nature* **451**, 664–669 (2008).
- Wendin, G. Quantum information processing with superconducting circuits: a review. *Rep. Prog. Phys.* **80**, 106001 (2017).
- Blais, A., Grimsmo, A. L., Girvin, S. & Wallraff, A. Circuit quantum electrodynamics. *Rev. Mod. Phys.* **93**, 025005 (2021).



4. Pirandola, S. & Braunstein, S. L. Physics: Unite to build a quantum internet. *Nature* **532**, 169–171 (2016).
5. Chen, Y.-A. et al. An integrated space-to-ground quantum communication network over 4600 kilometres. *Nature* **589**, 214–219 (2021).
6. Lauk, N. et al. Perspectives on quantum transduction. *Quantum Sci. Technol.* **5**, 020501 (2020).
7. Han, X., Fu, W., Zou, C.-L., Jiang, L. & Tang, H. X. Microwave-optical quantum frequency conversion. *Optica* **8**, 1050–1064 (2021).
8. Lambert, N. J., Rueda, A., Sedlmeir, F. & Schwefel, H. G. Coherent conversion between microwave and optical photons—an overview of physical implementations. *Adv. Quantum Technol.* **3**, 1900077 (2020).
9. Andrews, R. W. et al. Bidirectional and efficient conversion between microwave and optical light. *Nat. Phys.* **10**, 321–326 (2014).
10. Arnold, G. et al. Converting microwave and telecom photons with a silicon photonic nanomechanical interface. *Nat. Commun.* **11**, 4460 (2020).
11. Mirhosseini, M., Sipahigil, A., Kalaee, M. & Painter, O. Superconducting qubit to optical photon transduction. *Nature* **588**, 599–603 (2020).
12. Jiang, W. et al. Efficient bidirectional piezo-optomechanical transduction between microwave and optical frequency. *Nat. Commun.* **11**, 1166 (2020).
13. Forsch, M. et al. Microwave-to-optics conversion using a mechanical oscillator in its quantum ground state. *Nat. Phys.* **16**, 69–74 (2020).
14. Han, X. et al. Cavity piezo-mechanics for superconducting-nanophotonic quantum interface. *Nat. Commun.* **11**, 3237 (2020).
15. Zhang, X., Zhu, N., Zou, C.-L. & Tang, H. X. Optomagnonic whispering gallery microresonators. *Phys. Rev. Lett.* **117**, 123605 (2016).
16. Hisatomi, R. et al. Bidirectional conversion between microwave and light via ferromagnetic magnons. *Phys. Rev. B* **93**, 174427 (2016).
17. Zhang, X., Zou, C.-L., Jiang, L. & Tang, H. X. Strongly coupled magnons and cavity microwave photons. *Phys. Rev. Lett.* **113**, 156401 (2014).
18. Zhu, N. et al. Waveguide cavity optomagnonics for microwave-to-optics conversion. *Optica* **7**, 1291–1297 (2020).
19. Bartholomew, J. G. et al. On-chip coherent microwave-to-optical transduction mediated by ytterbium in  $\text{YVO}_4$ . *Nat. Commun.* **11**, 3266 (2020).
20. Adwaith, K., Karigowda, A., Manwatkar, C., Bretenaker, F. & Narayanan, A. Coherent microwave-to-optical conversion by three-wave mixing in a room temperature atomic system. *Opt. Lett.* **44**, 33–36 (2019).
21. Vogt, T. et al. Efficient microwave-to-optical conversion using rydberg atoms. *Phys. Rev. A* **99**, 023832 (2019).
22. O'Brien, C., Lauk, N., Blum, S., Morigi, G. & Fleischhauer, M. Interfacing superconducting qubits and telecom photons via a rare-earth-doped crystal. *Phys. Rev. Lett.* **113**, 063603 (2014).
23. Fernandez-Gonzalvo, X., Chen, Y.-H., Yin, C., Rogge, S. & Longdell, J. J. Coherent frequency up-conversion of microwaves to the optical telecommunications band in an er: Yso crystal. *Phys. Rev. A* **92**, 062313 (2015).
24. Holzgrafe, J. et al. Cavity electro-optics in thin-film lithium niobate for efficient microwave-to-optical transduction. *Optica* **7**, 1714–1720 (2020).
25. Javerzac-Galy, C. et al. On-chip microwave-to-optical quantum coherent converter based on a superconducting resonator coupled to an electro-optic microresonator. *Phys. Rev. A* **94**, 053815 (2016).
26. Fu, W. et al. Cavity electro-optic circuit for microwave-to-optical conversion in the quantum ground state. *Phys. Rev. A* **103**, 053504 (2021).
27. Xu, Y. et al. Bidirectional interconversion of microwave and light with thin-film lithium niobate. *Nat. Commun.* **12**, 4453 (2021).
28. McKenna, T. P. et al. Cryogenic microwave-to-optical conversion using a triply resonant lithium-niobate-on-sapphire transducer. *Optica* **7**, 1737–1745 (2020).
29. Soltani, M. et al. Efficient quantum microwave-to-optical conversion using electro-optic nanophotonic coupled resonators. *Phys. Rev. A* **96**, 043808 (2017).
30. Tsang, M. Cavity quantum electro-optics. *Phys. Rev. A* **81**, 063837 (2010).
31. Tsang, M. Cavity quantum electro-optics. II. Input-output relations between traveling optical and microwave fields. *Phys. Rev. A* **84**, 043845 (2011).
32. Wang, C. et al. Integrated lithium niobate electro-optic modulators operating at cmos-compatible voltages. *Nature* **562**, 101–104 (2018).
33. Fan, L. et al. Superconducting cavity electro-optics: a platform for coherent photon conversion between superconducting and photonic circuits. *Sci. Adv.* **4**, earr4994 (2018).
34. Zhang, M., Wang, C., Cheng, R., Shams-Ansari, A. & Lončar, M. Monolithic ultra-high-Q lithium niobate microring resonator. *Optica* **4**, 1536–1537 (2017).
35. Sahu, R. et al. Quantum-enabled operation of a microwave-optical interface. *Nat. Commun.* **13**, 1276 (2022).
36. Mobassem, S. et al. Thermal noise in electro-optic devices at cryogenic temperatures. *Quantum Sci. Technol.* **6**, 045005 (2021).
37. Hease, W. et al. Bidirectional electro-optic wavelength conversion in the quantum ground state. *PRX Quantum* **1**, 020315 (2020).
38. Rueda, A., Hease, W., Barzanjeh, S. & Fink, J. M. Electro-optic entanglement source for microwave to telecom quantum state transfer. *Npj Quantum Inf.* **5**, 1–11 (2019).
39. Rueda, A. et al. Efficient microwave to optical photon conversion: an electro-optical realization. *Optica* **3**, 597–604 (2016).
40. Romanenko, A. et al. Three-dimensional superconducting resonators at  $T < 20$  mk with photon lifetimes up to  $\tau = 2$  s. *Phys. Rev. Appl.* **13**, 034032 (2020).
41. Berlin, A. et al. Searches for new particles, dark matter, and gravitational waves with srf cavities. *arXiv preprint arXiv:2203.12714* (2022).
42. Alam, M. S. et al. Quantum computing hardware for hep algorithms and sensing. *arXiv preprint arXiv:2204.08605* (2022).
43. Romanenko, A. & Schuster, D. Understanding quality factor degradation in superconducting niobium cavities at low microwave field amplitudes. *Phys. Rev. Lett.* **119**, 264801 (2017).
44. Lambert, N., Trainor, L. & Schwefel, H. An ultra-stable microresonator-based electro-optic dual frequency comb. *arXiv preprint arXiv:2108.11140* (2021).
45. McRae, C. R. H. et al. Materials loss measurements using superconducting microwave resonators. *Rev. Sci. Instrum.* **91**, 091101 (2020).
46. Goryachev, M., Kostylev, N. & Tobar, M. E. Single-photon level study of microwave properties of lithium niobate at millikelvin temperatures. *Phys. Rev. B* **92**, 060406 (2015).
47. Yang, R.-Y., Su, Y.-K., Weng, M.-H., Hung, C.-Y. & Wu, H.-W. Characteristics of coplanar waveguide on lithium niobate crystals as a microwave substrate. *J. Appl. Phys.* **101**, 014101 (2007).
48. Cai, M., Painter, O. & Vahala, K. J. Observation of critical coupling in a fiber taper to a silica-microsphere whispering-gallery mode system. *Phys. Rev. Lett.* **85**, 74 (2000).
49. Serniak, K. et al. Hot nonequilibrium quasiparticles in transmon qubits. *Phys. Rev. Lett.* **121**, 157701 (2018).
50. Zmuidzinas, J. Superconducting microresonators: Physics and applications. *Annu. Rev. Condens. Matter Phys.* **3**, 169–214 (2012).
51. Delaney, R. et al. Superconducting-qubit readout via low-backaction electro-optic transduction. *Nature* **606**, 489–493 (2022).
52. Koch, J. et al. Charge-insensitive qubit design derived from the cooper pair box. *Phys. Rev. A* **76**, 042319 (2007).
53. Place, A. P. et al. New material platform for superconducting transmon qubits with coherence times exceeding 0.3 milliseconds. *Nat. Commun.* **12**, 1779 (2021).
54. Zhong, C. et al. Proposal for heralded generation and detection of entangled microwave–optical-photon pairs. *Phys. Rev. Lett.* **124**, 010511 (2020).
55. Krastanov, S. et al. Optically heralded entanglement of superconducting systems in quantum networks. *Phys. Rev. Lett.* **127**, 040503 (2021).
56. Heeres, R. W. et al. Cavity state manipulation using photon-number selective phase gates. *Phys. Rev. Lett.* **115**, 137002 (2015).
57. Chakram, S. et al. Seamless high-Q microwave cavities for multimode circuit quantum electrodynamics. *Phys. Rev. Lett.* **127**, 107701 (2021).
58. Nazmiev, A. I., Matsko, A. B. & Vyatchanin, S. P. Back action evading electro-optical transducer. *JOSA B* **39**, 1103–1110 (2022).
59. Zhong, C., Han, X. & Jiang, L. Quantum transduction with microwave and optical entanglement. *arXiv preprint arXiv:2202.04601* (2022).
60. Lecocq, F. et al. Control and readout of a superconducting qubit using a photonic link. *Nature* **591**, 575–579 (2021).

## ACKNOWLEDGEMENTS

This manuscript has been authored by Fermi Research Alliance, LLC under Contract No. DE-AC02-07CH11359 with the U.S. Department of Energy, Office of Science, Office of High Energy Physics. This work is funded by Fermilab's Laboratory Directed Research and Development (LDRD) program. This research used resources of the U.S. Department of Energy, Office of Science, National Quantum Information Science Research Centers, Superconducting Quantum Materials and Systems Center (SQMS) under contract number DE-AC02-07CH11359. The NQI Research Center SQMS contributed by supporting the design of SRF cavities and access to facilities. The authors would like to thank Johannes Fink for the insightful discussions and feedback on topics related to this paper.

## AUTHOR CONTRIBUTIONS

C.W. carried out the numerical analysis and optical simulations, coordinated the microwave-optical design, and drafted the manuscript. S.Z. conceived the project, coordinated the research, and helped draft and edit the manuscript. I.G. conducted microwave simulations and analysis. S.K. performed calculations and, along with V.Y., contributed to the conceptual design. A.G. and A.R. contributed to the final version of the manuscript. All authors gave their final approval for publication.

## COMPETING INTERESTS

The authors declare no competing interests.

**ADDITIONAL INFORMATION**

**Supplementary information** The online version contains supplementary material available at <https://doi.org/10.1038/s41534-022-00664-7>.

**Correspondence** and requests for materials should be addressed to Silvia Zorzetti.

**Reprints and permission information** is available at <http://www.nature.com/reprints>

**Publisher's note** Springer Nature remains neutral with regard to jurisdictional claims in published maps and institutional affiliations.



**Open Access** This article is licensed under a Creative Commons Attribution 4.0 International License, which permits use, sharing, adaptation, distribution and reproduction in any medium or format, as long as you give appropriate credit to the original author(s) and the source, provide a link to the Creative Commons license, and indicate if changes were made. The images or other third party material in this article are included in the article's Creative Commons license, unless indicated otherwise in a credit line to the material. If material is not included in the article's Creative Commons license and your intended use is not permitted by statutory regulation or exceeds the permitted use, you will need to obtain permission directly from the copyright holder. To view a copy of this license, visit <http://creativecommons.org/licenses/by/4.0/>.

© The Author(s) 2022